RSC Advances

PAPER

View Article Online
View Journal | View Issue

Cite this: *RSC Adv.*, 2015, **5**, 66367

Excitation dependent recombination studies on SnO_2/TiO_2 electrospun nanofibers†

Veluru Jagadeesh babu,*[a] Sesha Vempati,*[a] Yelda Ertas[ab] and Tamer Uyar*[ab]

Received 25th May 2015
Accepted 28th July 2015

DOI: 10.1039/c5ra09787h

www.rsc.org/advances

Poly(vinyl acetate) (PVAc)/TiO_2 nanofibers, PVAc/SnO_2 nanoribbons and PVAc/SnO_2–TiO_2 nanoribbons were produced *via* electrospinning. TiO_2 nanofibers and SnO_2 nanoribbons were obtained by removal of the polymeric matrix (PVAc) after calcination at 450 °C. Interestingly, PVAc/SnO_2–TiO_2 nanoribbons were transformed into SnO_2–TiO_2 nanofibers after calcination under the similar conditions. Fiber morphology and elemental mapping confirmed through SEM and TEM microscope techniques respectively. The X-ray diffraction measurements suggested the presence of anatase TiO_2 and rutile SnO_2 and both were present in the SnO_2–TiO_2 mixed system. Systematic photoluminescence studies were performed on the electrospun nanostructures at different excitation wavelengths (λ_{ex1} = 325, λ_{ex2} = 330, λ_{ex3} = 350, λ_{ex4} = 397 and λ_{ex5} = 540 nm). We emphasize that the defects in the SnO_2–TiO_2 based on the defect levels present in TiO_2 and SnO_2 and anticipate that these defect levels may have great potential in understanding and characterizing various semiconducting nanostructures.

Introduction

1D nanostructures *via* electrospinning have attracted significant attention due to the fact that their distinctive surface and quantum effects can influence the functionality and performance in nanodevices.[1–5] Among semiconductors, SnO_2 and TiO_2 have evoked considerable attention due to their potential applications in optoelectronic devices,[6–8] despite the anatase phase of TiO_2 being more photoactive.[9] It has been found that a combination of SnO_2 and TiO_2 gives the most significant sensing and photocatalytic applications.[10,11] In addition, SnO_2 and TiO_2 have a large bandgap (3.2 eV for anatase TiO_2 and 3.6 eV for SnO_2)[12,13] which ensures that the electrons within the conduction band (CB) have a strong reducing ability and the holes in the valence band (VB) have a strong oxidizing ability.[14] The impurities or defect states induced by the synthesis methods can form deep energy levels (which act as trapping centres) or shallow energy levels (which act as donors).[15] These shallow trap levels (lying in the bandgap) act as carrier traps in competition with the fast carrier recombination in the bulk during photoexcitation, which enhances the photoactivity of the nanostructures. On the other hand, Zhu *et al.*[16] reported that by considering chemical potentials, the deep trap levels exhibited reduced photocatalytic activities. Titania is a highly ionic lattice[17] with a VB composed of oxygen 2p orbitals (the wave functions are considerably localized on the O^{2-} lattice site), while the CB consists mostly of excited states of Ti^{4+}. The width of the VB in O^{2-} 2p is about 16 eV and the breadth of the CB in Ti^{4+} 3d is about 27 eV.[18]

Optical spectroscopy studies have been used extensively for the detection of CB electrons, trapped electrons, holes, and transition energy levels. Ghosh *et al.*[14] reported that the rutile TiO_2 single crystal consists of at least eight shallow trap levels (<1 eV below the CB). Later, the midgap energy related defects were identified from surface or bulk trap state luminescence either by surface modification of TiO_2 nanoparticles with a loading of platinum[19] or by treatment with $TiCl_4$.[20] Ariga *et al.*[21] demonstrated that photo-oxidation on the TiO_2 (001) surface has a threshold energy between 2.1 and 2.3 eV (539–590 nm), which is apparently much lower than that of the bandgap energy (3.0–3.2 eV). The two defect related bands were observed in titanate nanostructures (at 463 and 533 nm)[22] and assigned to carrier trapping at defect centers. On the other hand, the optical properties of SnO_2 are of great importance because of the even parity symmetry which precludes from the band-edge radiation transition.[23] Upon reducing the dimensionality of the SnO_2 crystals, the wave function symmetry can be broken due to quantum confinement and hence the dipole forbidden selection rule can be relieved, giving rise to the free exciton emission.[24] The luminescence would be dependent on the shape of the nanostructures such as the fishbone-like nanoribbons of SnO_2 that exhibit green emission.[25] Luo *et al.*[26] performed temperature dependent PL on SnO_2 nanowires and nanobelts where two bands centered at 470 nm and 560 nm were observed with the intensity of the former band being strongly dependent

[a]*UNAM-National Nanotechnology Research Centre, Bilkent University, Ankara, 06800, Turkey. E-mail: vjbabu2002@gmail.com; svempati01@qub.ac.uk; uyar@unam.bilkent.edu.tr*

[b]*Institute of Materials Science & Nanotechnology, Bilkent University, Ankara, 06800, Turkey*

† Electronic supplementary information (ESI) available. See DOI: 10.1039/c5ra09787h

on temperature. Blue/violet emission was also reported for different shapes of SnO_2 nanocauliflowers, nanoblades, and other types of nanostructures.[27–30] Kar *et al.*[31] reported the morphology dependent luminescence for SnO_2 nanorods and nanoparticles. The exciton binding energy of SnO_2 is as large as 130 meV, which envisages efficient exciton emission at room temperature and even at higher temperatures. Kılıç and Zunger[32] observed five intrinsic defects coexisting in SnO_2, which are oxygen vacancies (V_O), tin vacancies (V_{Sn}), tin antisite defects (Sn_O), oxygen interstitial sites (O_i) and tin interstitial sites (Sn_i). Sn_i and V_O are the predominant defect structures in SnO_2 due to the multivalency of tin. These defect structures can produce shallow donor levels that cause n-type conduction which originates from the V_O, where the V_O can capture electrons which leads to singly ionized vacancies (V_O^+) or doubly ionized vacancies (V_O^{++}). However, there are inadequate reports on electrospun SnO_2/TiO_2 nanofibers with excitation dependent emission spectra analysis.

In the present study, the systematic excitation dependent photoluminescence (PL) on TiO_2, SnO_2 and SnO_2–TiO_2 electrospun nanofibers are conducted. The PL emission peaks are dependent on the bandgap and surface defects. The plausible band alignment is also proposed and discussed with respect to the excitation energy.

Experimental

Materials

All the chemicals were purchased and used without further purification: titanium(IV) isopropoxide (TIP, 97%, Sigma-Aldrich); tin(IV) chloride ($SnCl_4$, 99%, Sigma-Aldrich); poly(-vinyl acetate) (M_w: 350 000); methanol (99%, Sigma-Aldrich); and glacial acetic acid (100%, Merck).

Synthesis of the nanostructures

The preparation of nanostructures *via* electrospinning is a well-known technology.[33,34] The polymer solutions were prepared by dissolving 1.2 g of PVAc in 10 mL of methanol and stirring for ~3 h. For the TiO_2 preparation, 2 mL of glacial acetic acid was added to the polymer solution, followed by 1 mL TIP which was then subjected to stirring for ~6 h to obtain a clear and homogeneous solution. For the SnO_2 synthesis, 0.5 mL of $SnCl_4$ was added to the polymer solution (PVAc) and subjected to stirring for ~6 h. Whereas for the SnO_2–TiO_2 solution, 2 mL of glacial acetic acid, 1 mL TIP and 0.5 mL of $SnCl_4$ were added to the polymer solution (PVAc) and subjected to ~6 h of stirring.

The solution was taken in a 10 mL syringe (21 G 1/2 needle) and was placed in a commercially available electrospinning machine Nanoweb (Electrospin 100) for the preparation of the nanofibers. The flow rate was adjusted to 25 μL m^{-1} with a syringe pump (KD Scientific, KDS 101), the distance between the two electrodes (tip of the needle to collector) was maintained at 8 cm, and the applied voltage between the rotating drum collector (with a speed of 200 rpm) and the tip of the needle was 15 kV. The electrospun PVAc/TiO_2 nanofibers, PVAc/SnO_2 nanoribbons and PVAc/SnO_2–TiO_2 nanoribbons were then subjected to calcination at 450 °C for about 3 h. After calcination the samples are referred to in a short form as TNF, SNR and STNF, respectively.

Characterization

Thermal analysis was performed on the nanostructures using a thermogravimetric analyser (TGA, Q500, TA Instruments) in the range of room temperature (T_R) to 700 °C in a nitrogen atmosphere. The morphologies of the microstructures and nanostructures were observed by scanning electron microscopy (SEM, FEI-Quanta 200 FEG). Approximately 5 nm of Au/Pd was sputtered on the samples before they were subjected to SEM scanning. The nanofibers were examined using transmission electron microscopy (TEM, FEI-Tecnai G2 F30). The samples were dispersed in ethanol and a tiny drop was dried on a holey carbon coated TEM grid and analysed with energy dispersive X-ray spectroscopy (EDX) for elemental analysis. The crystal structures of the nanofibers were characterized using a PANalytical X'Pert Pro multipurpose X-ray diffractometer (XRD) in the range of $2\theta = 20–80°$ with CuKα (1.5418 Å) radiation. UV-vis absorbance spectroscopy of the nanostructures was performed using a UV-vis spectrometer (VARIAN, Cary 5000) by taking nearly 1–5 mg of dispersion in a quartz cuvette. PL measurements were performed on the fibers as free standing flakes in the PL spectrometer (Jobin Yvon, FL-1057 TCSPC) at different excitation wavelengths ($\lambda_{ex1} = 325$, $\lambda_{ex2} = 330$, $\lambda_{ex3} = 350$, $\lambda_{ex4} = 397$ and $\lambda_{ex5} = 540$ nm). The XRD peaks and PL emission peaks were deconvoluted with a Lorentz and Gauss fitting respectively, with Origin 8.5 where it was necessary.

Results and discussion

Surface morphology

The surface morphology of the nanostructures was observed by SEM and is shown in Fig. 1. The as-spun nanostructures of PVAc/TiO_2, PVAc/SnO_2, and PVAc/SnO_2–TiO_2 exhibit fiber (Fig. 1a), ribbon (Fig. 1c) and ribbon (Fig. 1e) like structures and after calcination they are denoted as TNF, SNR and STNF, respectively. However, all these nanostructures are smooth and bead-free. That is to say, the charges (viscoelastic force and electrostatic repulsion) between the precursor solutions were successfully balanced by controlling the process parameters (humidity, flow rate, substrate rotation speed and high voltage) to suppress the influence of surface tension which drives the bead formation.[35,36]

The calcination of the as-spun nanostructures was carried out at 450 °C. The successful removal of the polymeric part from the PVAc/TiO_2, PVAc/SnO_2 and PVAc/SnO_2–TiO_2 nanostructures was first confirmed by TGA studies. The main weight loss occurs between 100 and 400 °C due to the decomposition of the polymeric matrix (PVAc) and organic content of the precursors present in the as-spun nanostructures (Fig. SI-1†). Interestingly, after calcination, the morphology of TNF (Fig. 1b) and SNR (Fig. 1d) remains unchanged, whereas PVAc/SnO_2–TiO_2 is converted to fiber shaped STNF (Fig. 1f) and the fibers are uniform throughout their lengths. The decrease in dimensions after

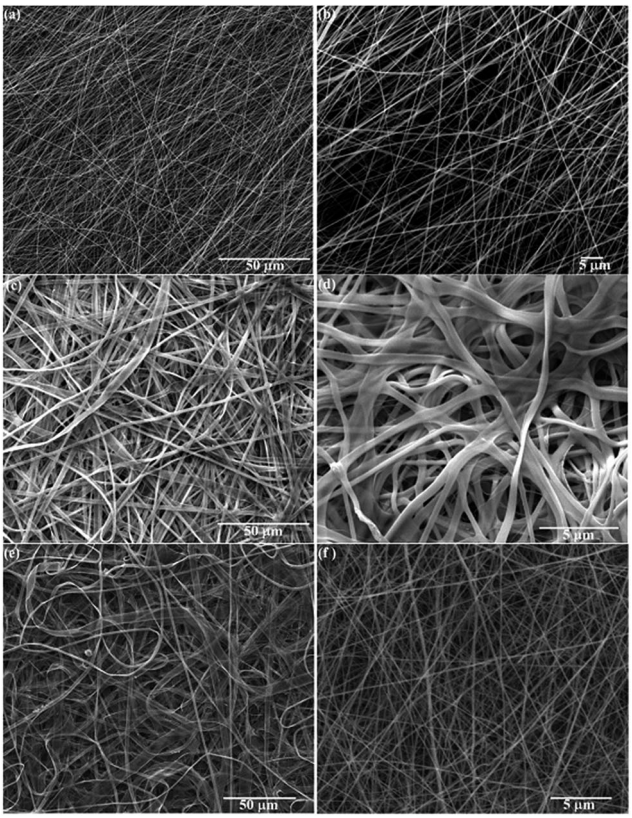

Fig. 1 SEM images of the as-spun nanostructures of (a) PVAc/TiO_2, (c) PVAc/SnO_2, (e) PVAc/SnO_2–TiO_2 and after calcination (b) TNF, (d) SNR and (f) STNF at 450 °C.

calcination and the rougher surface is due to the loss of organic substances and crystallization during the thermal treatment.[37] The average dimensions of the nanostructures with their standard deviation are presented (see Fig. SI-2 and Table SI-1†) for a clear estimation. The possible mechanism for the transformation of ribbons into fibers is most likely to be 'wrapping of sheet' because of mechanical stress[38] arising during the crystallization/dissolution. Generally when a surface experiences an asymmetrical stress the excess surface energy results in wrapping or scrolling.[39] Ma *et al.*[40] evidenced the direct rolling of nanosheets into nanotubes of single layered titanates along the (010) axis. In single layered nanosheets, the interaction energy between atoms mostly lies in the same layer hence the sheets grow at the edges of the individual layers, rather than creating a new layer,[41] *i.e.* the interaction energy between the atoms of inter-layers was less than that between intra-layer atoms, which differs as much as 500 times. Apart from this, in the presence of an asymmetrical chemical environment[39] the excess surface energy causes bending and/or curving. Therefore the gain in surface energy is sufficient to convert nanoribbons into nanofibers.

From the TEM image presented in Fig. 2a it is evident that the nanostructures of STNF are composed of crystalline nanoparticles along the length of the fiber. Fig. 2b, at a higher magnification, depicts the grains of the nanofiber. The lattice resolved image is shown in Fig. SI-3† where one can identify the lattice patterns of TiO_2 and SnO_2. The EDX spectrum in Fig. 2c confirms the presence of Ti, Sn and O components in the STNF fibers. While the inset of Fig. 2c represents the elemental mapping of TEM micrographs, which confirms that the Ti, Sn and O spatial distributions overlap in the selected region.

Crystal structure

XRD patterns of the nanofibrous structures are shown in Fig. 3. The diffraction peaks related to TNF are indexed and confirmed to be the anatase (A) phase according to the JCPDS file no. 21-1272, as presented in Fig. 3a. There are no indications of the peaks related to impurities or other phases like rutile/brookite within the detection limits of the XRD. The anatase phase is still predominant at 450 °C while a complete transformation was observed to occur at 750 °C from the literature.[42,43] In the case of SNR the peaks are indexed according to the JCPDS file no. 72-1147 confirming the rutile SnO_2 phase which is consistent with the literature.[44–46] The XRD pattern related to STNF is presented in Fig. 3a. It is important to note that the presence of SnO_2 hinders the growth of TiO_2 linkage which results in the formation of smaller crystallites (see Table 1). This is confirmed by the broadened XRD peaks with respect to TNF and SNR. That is why there are no well resolved peaks identified for STNF. As shown in Fig. 3b, the corresponding peaks are identified. From Fig. 3b, the rutile phase ratio is higher than SnO_2 and anatase TiO_2. Competition between the multiple phase elements might lead to a dominate rutile phase in STNF. Since both of these systems are tetragonal crystals, the lattice parameters and *d*-spacing values are determined using the equation given in ref. 47.

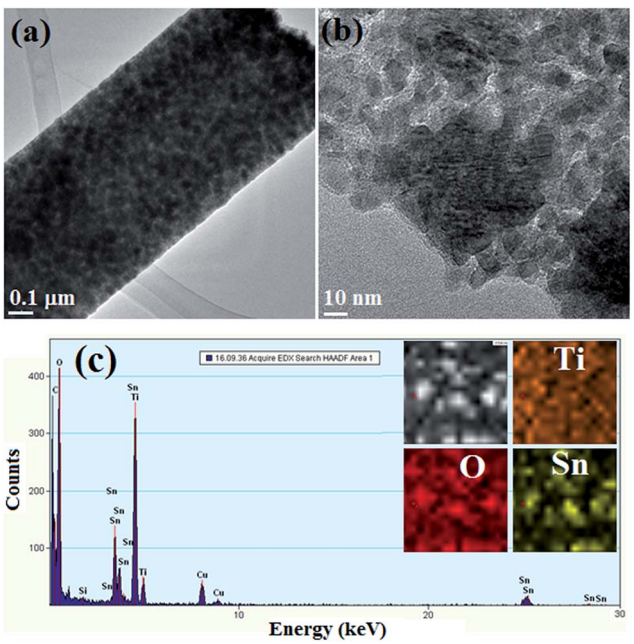

Fig. 2 (a) TEM image of a single nanofiber composed of STNF, (b) a higher magnification TEM and (c) EDX spectrum and elemental mapping images of TEM micrographs for STNF.

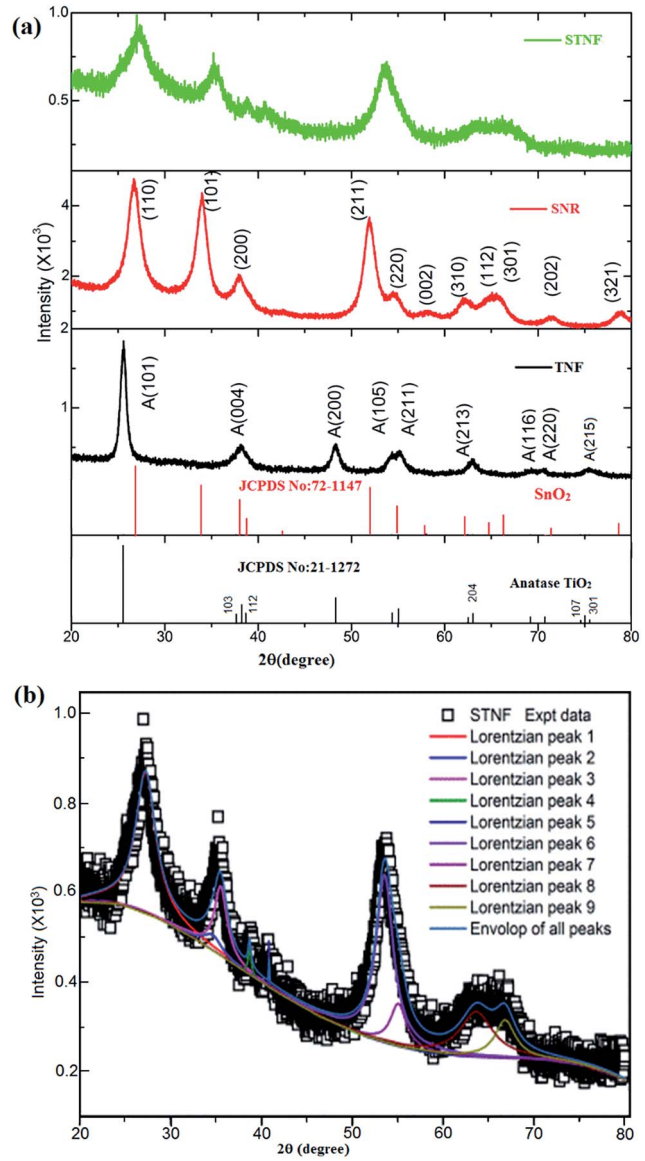

Fig. 3 X-ray diffraction profiles of (a) TNF, SNR and STNF and (b) STNF decomposed using Lorentz fitting. XRD patterns are indexed according to JCPDS file no. 21-1272 and JCPDS file no. 72-1147 for anatase TiO_2 and SnO_2 respectively.

From Fig. 4, the full width at half maximum (FWHM) of the diffraction peaks are obtained. The FWHM values and the crystallite sizes (d_{hkl}) were calculated through the Debye–Scherrer formula.[48] The calculated crystallite sizes of individual TNF, SNR and STNF are presented in Table 1. The crystallite sizes of STNF are smaller than those of the individual systems. However, by changing the calcination environment to either O_2 or under vacuum does not cause any influence on the crystalline sizes.[49] It is noted that at all Bragg reflections assigned to the tetragonal phase, a shift to slightly higher 2θ values from the STNF system is seen. This might be due to the lattice compression/expansion during calcination. Furthermore, the surface area (S_a) of the nanostructures is also calculated by eqn (1):[50,51]

$$S_a = \frac{6}{d_{hkl} \times \rho} \quad (1)$$

where the molecular density (ρ) is obtained from eqn (2):

$$\rho = \frac{nM}{NV} \quad (2)$$

where n represents the number of formula units per unit cell (4 for anatase and 2 for SnO_2), M is the molecular weight, N is Avogadro's number, and V is the volume of the unit cell. The higher the surface area is, the lower the activation energy is, which precludes the phase transformation below a certain temperature.[50]

Two types of doping, *viz.* (a) interstitial and (b) substitutional, can be expected depending on the electronegativity and ionic radius. For the first one, if the electronegativity (on the Pauling scale) of Sn^{4+} is closer to that of Ti^{4+} and the ionic radius (in Å) of Sn^{4+} is smaller than that of Ti^{4+}, then the lattice spacing will become larger. Then the doping ion will enter into the crystal cell of the oxide. While for the second one, if the electronegativity and ionic radius of the doping metal ions match those of the lattice metal ions in oxides, the doping metal ion will substitute itself for the lattice metal ion in the doping reactive process.[52] Since the difference in electronegativity of Sn^{4+} (1.96) and Ti^{4+} (1.54) results in a change in the volume of STNF, it could be expected that Sn^{4+} will replace Ti^{4+} in the lattice and occupy the Ti^{4+} positions by substitutional doping. Therefore, the volume of the unit cell (see Table 1) of STNF is moderately between that of TNF and SNR. In addition, the ionic radius of Sn^{4+} (0.71 Å)[53] is larger than that of the Ti^{4+} (0.68 Å)[53] ion, which will induce lattice distortions in STNF. From Table 1, the volume of the unit cell is very consistent, which indicates that the lattice would relax as Sn^{4+} ions with a larger ionic radius are substituted for Ti^{4+} in TiO_2.

Table 1 From the XRD data of TNF, SNR and STNF, where a, b, and c, are the lattice parameters, V, is the volume of the cell, S_a is the surface area, and d is the crystallite size

	Lattice parameters (Å)			$V = a^2 \times c$ (Å^3)	V per molecule (Å^3)	d (nm)	S_a (m^2 g^{-1})	Peak positions			
	$a = b$	c	c/a								
TNF-A	3.7595	9.4189	2.505	133.125	33.281	11.14	135.19				
SNR	4.7208	3.1845	0.6745	70.967	35.484	7.50	214				
STNF-A								38.687 (112)	53.560 (105)		
STNF-R	4.6288	3.0189	0.6521	64.682	32.341	3.179	460.24	27.245 (110)	35.500 (101)	40.796 (111)	63.672 (301)
STNF-SnO_2	4.7157	3.0999	0.6573	68.937	34.469	3.563	231.92	34.627 (101)	55.081 (220)	66.832 (301)	

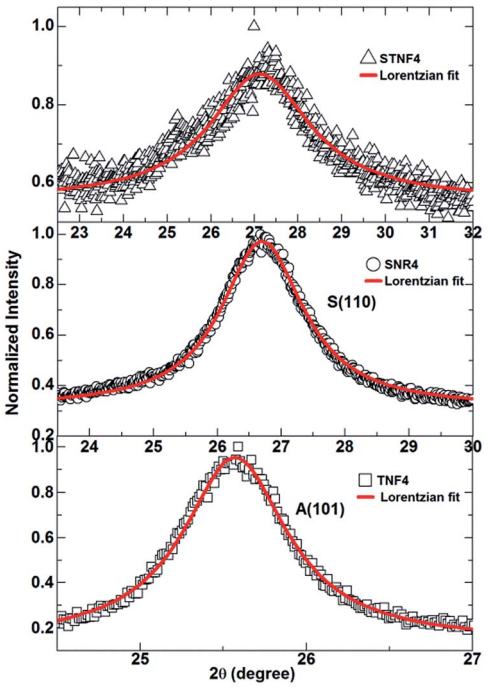

Fig. 4 Line-widths of TNF: A(101), SNR: S(110), and mixed phase STNF. The curves are fitted to the Lorentz distribution.

The lattice strain has been calculated using a Williamson–Hall (W–H) plot, using the following eqn (3):[54]

$$\frac{\beta \cos\theta}{\lambda} = \frac{1}{D} + \frac{\eta \sin\theta}{\lambda} \quad (3)$$

where η is the strain, and D is the effective crystallite size. The relation between $\beta \cos\theta$ and $\sin\theta$ indicates whether the sample is subjected to compressive stress or tensile strain during the thermal treatment. The W-H plots for the samples are presented in the Fig. SI-4†, it reveals that TNF exhibits compressive stress.[55] Whereas, SNR and STNF disclose positive slopes suggesting that both of them undergo tensile strain. The intercepts on the $\beta \cos\theta$ axes give the effective crystallite sizes corresponding to zero strain.[51]

UV-vis absorption

Optical absorption spectra for the nanostructures were recorded and are shown in Fig. 5. The absorption bands of TNF exhibit a peak maxima at 372 nm (3.33 eV). There are no identifications related to impurities/structural defects, and possibly no absorption is observed in the visible region. This strong absorption peak at 372 nm is due to the band-to-band transition.[56] Ghosh *et al.*[14] reported that the onset and band edges occuring at 3.17 and 3.02 eV are due to indirect transitions in rutile TiO_2, but they are not related to the occupancy of the shallow trap states. In the present study there are no sharp bands observed for SNR and STNF, in contrast with the literature.[56,57] The synthesis methods and structural changes can affect the electronic and optical properties of the STNF band edge[56,58] and effect coupling[59] between the TNF and SNR system. Introduction of SnO_2 into the TiO_2 lattice may induce changes in the light absorption properties. STNF exhibits distinct features from TNF and SNR. Since the doping energy level of Sn^{4+} is located at 0.4 eV below the CB of Ti^{4+}, it helps to shift the wavelength to lower regions[52,56] in STNF. The bandgap of STNF eventually falls below the bandgap of anatase TiO_2. These changes in the optical bandgap indicate a slight reorganization of the energy band structures[60] in STNF, compared to the pristine individual systems. Upon the introduction of SnO_2 into TiO_2, the optical absorption properties of STNF exhibit a blue shift.[11,61] In addition, the conversion of shape (nanoribbons to nanofibers) lead to a change in the fundamental absorption edge.[51] Despite the presence of SnO_2 in TiO_2, negligible effects were also reported in the electronic properties of TiO_2 with a lower amount of guest ion introduction.

Photoluminescence

The room temperature PL spectra for the electrospun nanostructures were recorded at different excitation wavelengths: $\lambda_{ex1} = 325$, $\lambda_{ex2} = 330$, $\lambda_{ex3} = 350$, $\lambda_{ex4} = 397$ and $\lambda_{ex5} = 540$ nm, presented in Fig. SI-5†. The PL spectra of TNF are shown in Fig. 6, but for better clarity they are plotted in two ranges as 350 to 520 nm (R_1) in Fig. 6a and 450 to 800 nm (R_2) in Fig. 6b. In R_1 (λ_{ex1}, λ_{ex2}, λ_{ex3} and λ_{ex4}) four emission peaks P_1^T, P_2^T, P_3^T, and P_4^T at 383, 408, 435 and 487 nm respectively are observed. Zhu *et al.*[16] reported the energy defect levels within the anatase TiO_2 nanocrystals by the optical transient infrared absorption spectroscopy method, and then considered the chemical potentials that enhanced the photo response. The onset of absorption at P_1^T corresponds to the bandgap energy of anatase TiO_2. Serpone *et al.*[62] reported that the band at 383 nm is assigned to the highest energy indirect transition $X_{1b} \rightarrow \Gamma_3$ (where X and Γ denote the edge and center of the Brillouin zone (BZ)). The

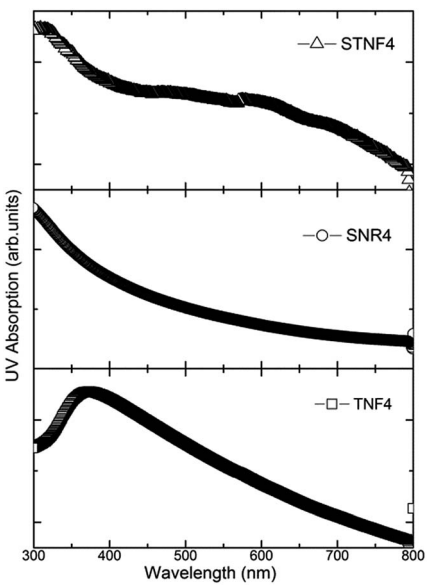

Fig. 5 Optical absorption spectra for TNF, SNR and STNF nanostructures.

peaks at P_2^T and P_3^T are ascribed to $X_{2b} \rightarrow \Gamma_{1b}$, and $X_{1a} \rightarrow \Gamma_{1b}$ respectively, which are the lowest energy allowed indirect phonon assisted transitions. The emission peak at P_4^T is assigned to the shallow trap level.[62] In R_2 (λ_{ex1}, λ_{ex2}, λ_{ex3}, λ_{ex4} and λ_{ex5}, Fig. 6b) two emission peaks P_5^T and P_6^T at 562 nm (2.21 eV) and 585 nm (2.12 eV) respectively are identified. The band in the visible region at P_5^T is attributed to the radiative recombination of self-trapped excitons.[63,64] The TNF surface exhibits an emission band at P_5^T (~2.2 eV) which is apparently much lower than that of the bandgap energy (3.0 eV for rutile and 3.2 eV for anatase TiO_2).[16,62] These P_5^T and P_6^T peaks belong to shallow traps with V_O at 0.99 eV and 1.08 eV below the CB. The shallow traps most likely concern V_O at various energies. The green emissions can be described by the following mechanism:[62]

$$TiO_2 \xrightarrow{h\nu} TiO_2(e^-/h^+) \rightarrow {e_{CB}}^- + {h_{VB}}^+ \quad (4)$$

$$V_O^0 + {e_{CB}}^- \rightarrow V_O \ (e^- \text{ trapping in shallow traps}) \quad (5)$$

$$V_O \rightarrow {h_{VB}}^+ \rightarrow V_O^0 + h\nu \ (\text{radiative recombination}) \quad (6)$$

where V_O^0 is an ionized oxygen vacancy level composed to rapidly trap (in tens to hundreds of femtoseconds) a photogenerated CB electron which subsequently interacts with a VB hole (trapped in less than a few picoseconds) either radiatively or non-radiatively. The dominant but not exclusive route for charge carrier recombination in small semiconductor particles is the non-radiative path because of strong coupling of the wave functions of trapped electrons and trapped holes with the lattice phonon.

PL emission spectra of SNR are shown in two ranges, *viz.* R_1 and R_2, in Fig. 6c and 6d respectively. Four emission peaks P_1^S, P_2^S, P_3^S and P_4^S located at 372, 406, 440 and 492 nm can be seen in range R_1 (Fig. 6c). It is noteworthy that bulk SnO_2 does not show luminescence, but at lower dimensions it does.[65,66] The peak at P_1^S with violet emission might be due to the near band edge emission.[31] Viana *et al.*[13] assigned a similar peak of P_1^S to the recombination of electrons from the CB to excitons bound to neutral D^0x.

Kim *et al.*[67] observed the peak at 416 nm (2.98 eV), but in the present study a broad peak at P_2^S is identified. The origin of this peak is ascribed to Sn_i resulting from the nanosized SnO_2 nanoribbon-like structures. The peak at P_3^S is the blue emission. Kar *et al.*[31] reported that the SnO_2 nanocrystals with larger sizes (26.6 nm) and nearly perfect crystalline structures exhibit stronger violet emission. This P_3^S emission ascribed as a luminescent centre due to electron transitions is mediated by defect levels in the bandgap, such as V_O and luminescent centers formed by such interstitial sites or dangling in the presence of SnO_2 nanocrystals.[45] The peak at P_4^S is a shallow trap level ~0.8 eV below the CB. Since the energy of the emission band is lower than the bandgap energy of SnO_2 ($E_g = 3.6$ eV),[13,68] the emission is not due to the direct recombination of a conduction electron in the 4p band of Sn and a hole in the 2p VB of O.[69] The peak at P_4^S is assigned to isolated ${V_O}^+$ centers, which lie at a higher energy than the complex ${V_O}^+$ center.[13] In range R_2 (see Fig. 6d), a broad orange emission peak is identified as P_5^S and

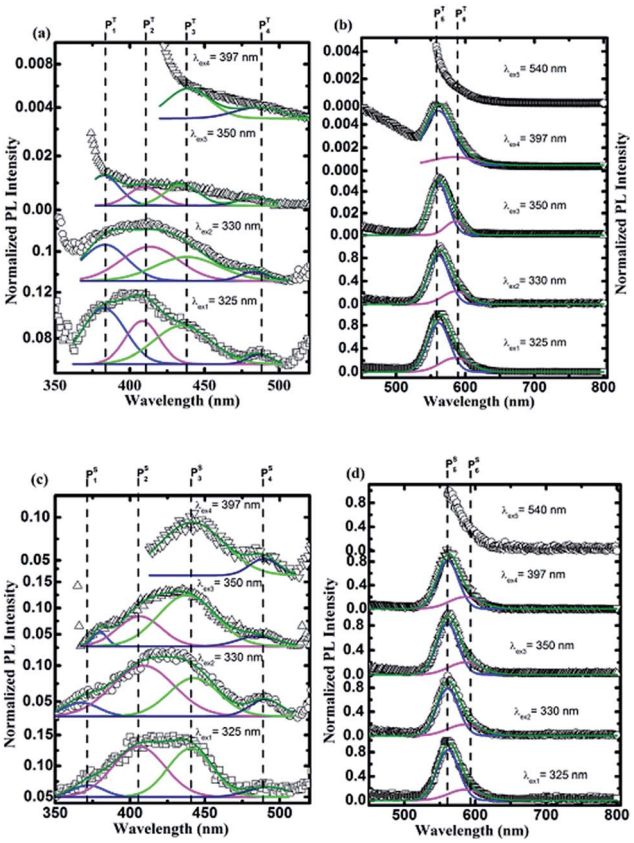

Fig. 6 Normalized PL emission spectra at different excitation wavelengths of (a) TNF in range R_1, (b) TNF in range R_2, (c) SNR in range R_1 and (d) SNR in range R_2.

P_6^S positioned at 562 and 585 nm. The P_5^S peak is attributed to the radiative recombination of self-trapped excitons, while the other peak at P_6^S was also observed by Gao and Wang.[70] Both of these peaks at P_5^S and P_6^S correspond to oxygen deficiency defects (V_O or Sn_i) in the SNR nanoribbons. Viana *et al.*[13] assigned the peak at 599 nm (2.07 eV) to ${V_O}^+$. In the present study the peak at P_6^S observed from the SNR nanoribbons is attributed to ${V_O}^+$. These midgap V_O states were defined by the broad and strong green peaks. The surface states are situated at 2.7 eV below the conduction band minimum (CBM) and 0.9 eV above the valence band maximum (VBM). The observed emission peaks (P_5^S and P_6^S from Fig. 6c and 6d) at 2.1 to 2.2 eV are less than the energy gap between the CBM and surface states (~2.7 eV).[68] The electrons from the CB are captured by shallow trap levels below the CB and then recombine with the holes at the surface states (2.7 eV below the CB).

The emission peak intensity with respect to the peak positions are listed (Fig. SI-6 and Table SI-2†). The higher the surface area of the nanostructures is, the greater the number of V_O is, which results in decreased PL peak intensities. For better comprehension, the integrated area under the peak plotted against the particular peak position is shown in Fig. 7. A_1^T, A_2^T, A_3^T, A_4^T, A_5^T and A_6^T represent the area under the peaks of P_1^T, P_2^T, P_3^T, P_4^T, P_5^T, and P_6^T respectively of TNF (see Fig. 7a). The area of the TNF nanofibers is changed but the position of the PL

peak does not change, indicating that the main PL peak is not the intrinsic feature of TiO_2. These minor changes in the peak positions might be due to the non-uniform distribution of the defect levels at nanodimensions. Similarly, A_1^S, A_2^S, A_3^S, A_4^S, A_5^S, and A_6^S describe the area under the peak positions at P_1^S, P_2^S, P_3^S, P_4^S, P_5^S and P_6^S respectively of SNR, as shown in Fig. 7b. Noticeable from both figures (Fig. 7a and 7b) is the increased peak area at P_5^T and P_5^S which may result from the increased number of oxygen defects in TNF and SNR. The blue emission is almost zero and only red emission is observed.

Fig. 8a shows the PL emission spectra of STNF, where the peak positions P_1^{ST}, P_2^{ST}, P_3^{ST}, P_4^{ST}, P_5^{ST} and P_6^{ST} are at 373, 412, 433, 488, 560 and 586 nm respectively. It is also known that the PL spectra of nanostructures are usually broad and often asymmetric. The degree of crystallinity improves with the increase of the calcination temperature above 400 °C. Hence the calcination temperature and tailored crystallization give rise to modified optical properties in the SNTF nanostructures. Since STNF has the higher surface area (see Table 1), V_O are easily formed in the nanofibers resulting in structural defects at Ti centres in the basic unit cell of STNF. The peaks at P_1^{ST}, P_2^{ST}, P_3^{ST} and P_4^{ST} show little variation when compared to TNF and SNR, which is because SnO_2 is substituted into the TiO_2 system. Interestingly, the peak positions at P_5^{ST} and P_6^{ST} are unchanged from TNF and SNR. The origin of the green emission (540–555 nm) in bulk materials is still debatable and some authors attribute it to V_O while others attributed it to Ti_i or Sn_i.[14,32] However, it is widely accepted that the origin of the green emission is assigned to the recombination of electrons in the single occupied V_O with photoexcited holes.[64,71,72] The area under the peaks A_1^{ST}, A_2^{ST}, A_3^{ST}, A_4^{ST}, A_5^{ST}, and A_6^{ST} positioned at P_1^{ST}, P_2^{ST}, P_3^{ST}, P_4^{ST}, P_5^{ST} and P_6^{ST} respectively of STNF is shown in Fig. 8b. As discussed earlier, A_5^T and A_5^S are dominant for TNF and SNR, whereas A_2^{ST} and A_4^{ST} are dominant for STNF, *i.e.* a blue shift has occurred. This blue shift in the peak position suggests that the increased oxygen defect states are starting to form even in the lower wavelength regions.

The proposed band alignment of the nanostructures is shown in Fig. 9. Fig. 9 exhibits six shallow energy bands for TNF and SNR. From Fig. 9 (the TNF part), it is suggested that for the excitations λ_{ex1}, λ_{ex2} and λ_{ex3} (3.82, 3.78 and 3.54 eV), electrons from the VB would be excited to the CB and populate all the six bands and recombine with holes at the VB. While for the excitation at λ_{ex4} (3.12 eV), the electrons will not reach even the CB, so there are four bands seen near to the CB. In the case of the λ_{ex5} (2.3 eV) excitation, the energy is 2.29 eV, hence only two bands are observed. From Fig. 9 (the SNR part), it is notable that for the excitations at λ_{ex1} and λ_{ex2}, the electron could be excited by more than the SnO_2 bandgap energy (3.6 eV) and at λ_{ex3} (3.54 eV) the electron is close to E_g, therefore, all of the six bands will be emitted. Whereas for λ_{ex4} and λ_{ex5}, only four and one band will be emitted respectively depending on their corresponding excitation energies. Band alignment of STNF is shown in Fig. 9, and once TiO_2 and SnO_2 contact each other to form a junction, band bending will occur at the interface to reach an equal Fermi

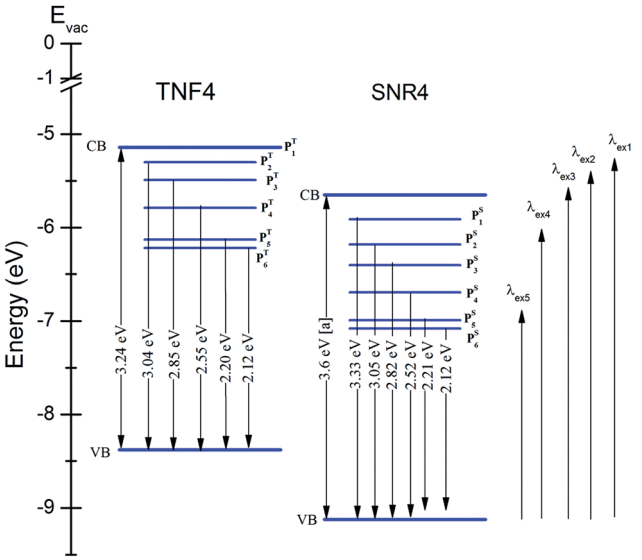

Fig. 9 Band alignment with respect to the vacuum energy level for STNF, where [a] represents the bandgap of SNR as from ref. 13 and 68.

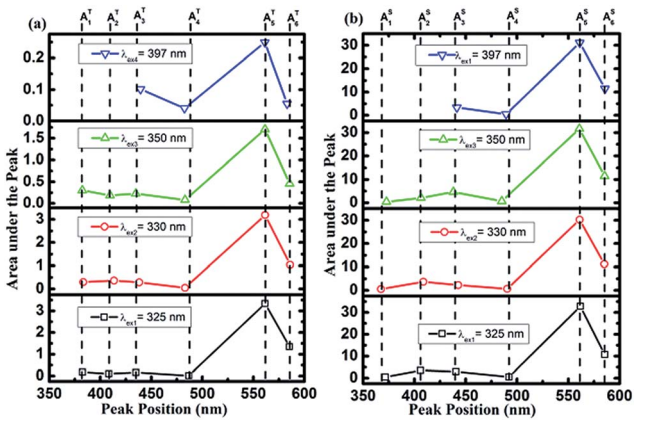

Fig. 7 Area under the peaks of (a) TNF and (b) SNR at different positions.

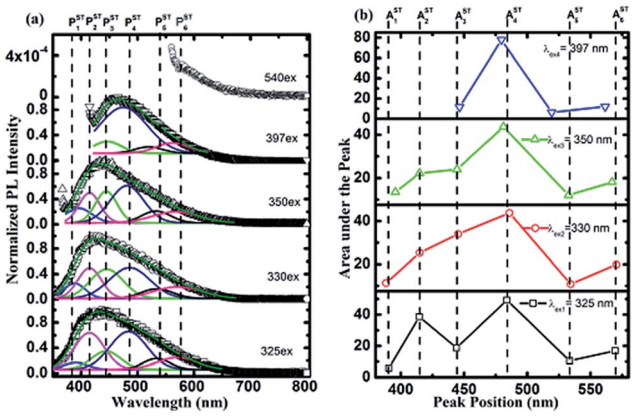

Fig. 8 (a) Normalized PL emission spectra of STNF in the range of 350 to 800 nm at different excitations (λ_{ex} = 325, 330, 350, 397 and 540 nm) and (b) area under the peaks for STNF.

level. When both parts of STNF are excited, electron transfer occurs from the CB of TiO_2 to the CB of SnO_2 and, conversely, holes transfer from the VB of SnO_2 to the VB of TiO_2. Thus the e^-/h^+ pairs are separated at the interface.[73] The band alignment for STNF is illustrated in Fig. 9. Since the λ_{ex1}, λ_{ex2} and λ_{ex3} excitation energies are higher than the bandgap energies of both parts, the electrons from the CB of TNF would be transferred to the all midgap bands of SNR. The populated emission bands are significant at these three excitations. With the excitation energy at λ_{ex4}, the electrons would be excited up to P_2^T of TNF and transfer to the P_2^S, P_3^S, P_4^S, P_5^S and P_6^S bands of SNR. While at λ_{ex5}, they can be excited up to P_5^T of TNF and transfer to the P_5^S and P_6^S bands of SNR.

Conclusions

Electrospun SnO_2–TiO_2 nanofibers were obtained after the calcination of nanoribbon-like structures. The morphologies and dimensions of the nanostructures were observed by SEM. The possible mechanism for the transformation of ribbons into fibers was confirmed and discussed with the literature as support.[38] XRD analysis revealed that both TNF and SNR belong to tetragonal phases and substitutional doping was confirmed. The W–H plots suggested that the lattice has undergone compressive stress/tensile strain. The UV-vis absorption spectra show a band-to-band transition at 372 nm (3.33 eV) for TNF. In the case of SNR and STNF no sharp bands were identified because of the induced structural changes from the synthesis which can affect the electronic and optical properties of the STNF band edge[56,58] and the effect of coupling[59] between the TNF and SNR system. Therefore, the optical absorption of STNF exhibited a blue shift. The change in morphology leads to a difference in the density of defects which was also observed from the PL spectra. The normalized PL peak exhibits six shallow trap energy levels and their origin is assigned with respect to the excitation wavelength. Band bending was also expected due to the difference in electronegativity of the host and substituent ions, since Sn substitutes for Ti. The integral peak area against the peak position shows that at P_5^T and P_5^S, a green emission is exhibited for TNF and SNR respectively, whereas STNF discloses a blue emission at P_2^{ST} and P_4^{ST}. The proposed band alignment for the electrospun nanostructures of STNF and the possible mechanism for the defect energy bands were elaborated. Apparently, these findings would have great potential in measuring the midgap levels of other semiconducting nanostructures. These investigations would attract much attention and they also require further theoretical explanation of the defect energy states in the STNF system.

Acknowledgements

V. J. B. and S. V. thank The Scientific & Technological Research Council of Turkey (TUBITAK) (TUBITAK-BIDEB 2221, Fellowships for Visiting Scientists and Scientists on Sabbatical) for fellowship. Y. E. thanks TUBITAK-BIDEB 2211 for the PhD student scholarship. T. U. thanks The Turkish Academy of Sciences – Outstanding Young Scientists Award Program (TUBA-GEBIP) for partial funding.

References

1 V. Lopez-Richard, J. C. González, F. M. Matinaga, C. Trallero-Giner, E. Ribeiro, M. R. S. Dias, L. Villegas-Lelovsky and G. E. Marques, *Nano Lett.*, 2009, **9**, 3129–3136.
2 M. C. Carotta, S. Gherardi, V. Guidi, C. Malagù, G. Martinelli, B. Vendemiati, M. Sacerdoti, G. Ghiotti, S. Morandi, A. Bismuto, P. Maddalena and A. Setaro, *Sens. Actuators, B*, 2008, **130**, 38–45.
3 V. J. Babu, S. R. S. Bhavatharini and S. Ramakrishna, *RSC Adv.*, 2014, **4**, 19251–19256.
4 V. J. Babu, S. Vempati, T. Uyar and S. Ramakrishna, *Phys. Chem. Chem. Phys.*, 2015, **17**, 2960–2986.
5 B. Sundaray, V. J. Babu, V. Subramanian and T. S. Natarajan, *J. Eng. Fibers Fabr.*, 2008, **3**, 39–45.
6 P. G. Harrison and M. J. Willett, *Nature*, 1988, **330**, 337–339.
7 R. Asahi, T. Morikawa, T. Ohwaki, K. Aoki and Y. Taga, *Science*, 2001, **293**, 269–271.
8 M. Law, H. Kind, B. Messer, F. Kim and P. Yang, *Angew. Chem., Int. Ed.*, 2002, **41**, 2405–2408.
9 V. J. Babu, R. P. Rao, A. S. Nair and S. Ramakrishna, *J. Appl. Phys.*, 2011, **110**, 064327.
10 M. Radecka, K. Zakrzewska and M. Rekas, *Sens. Actuators, B*, 1998, **47**, 194–204.
11 J. Lin, J. C. Yu, D. Lo and S. K. Lam, *J. Catal.*, 1999, **183**, 368–372.
12 D. O. Scanlon, C. W. Dunnill, J. Buckeridge, S. A. Shevlin, A. J. Logsdail, S. M. Woodley, C. R. A. Catlow, M. J. Powell, R. G. Palgrave, I. P. Parkin, G. W. Watson, T. W. Keal, P. Sherwood, A. Walsh and A. A. Soko, *Nat. Mater.*, 2013, **12**, 798–801.
13 E. R. Viana, J. C. González, G. M. Ribeiro and A. G. d. Oliveira, *J. Phys. Chem. C*, 2013, **117**, 7844–7849.
14 A. K. Ghosh, F. G. Wakim and R. R. Addiss Jr, *Phys. Rev.*, 1969, **184**, 979–988.
15 F. M. Hossain, G. E. Murch, L. Sheppard and J. Nowotny, *Defect Diffus. Forum*, 2006, **251–252**, 1–12.
16 M. Zhu, Y. Mi, G. Zhu, D. Li, Y. Wang and Y. Weng, *J. Phys. Chem. C*, 2013, **117**, 18863–18869.
17 A. H. Kahn and A. J. Leyendecker, *Phys. Rev.*, 1964, **135**, A1321–A1325.
18 N. Daude, C. Gout and C. Jouanin, *Phys. Rev. B: Solid State*, 1977, **15**, 3229–3235.
19 X. Wang, Z. Feng, J. Shi, G. Jia, S. Shen, J. Zhou and C. Li, *Phys. Chem. Chem. Phys.*, 2010, **12**, 7083–7090.
20 F. J. Knorr, D. Zhang and J. L. McHale, *Langmuir*, 2007, **23**, 8686–8690.
21 H. Ariga, T. Taniike, H. Morikawa, M. Tada, B. K. Min, K. Watanabe, Y. Matsumoto, S. Ikeda, K. Saiki and Y. Iwasawa, *J. Am. Chem. Soc.*, 2009, **131**, 14670–14672.
22 V. J. Babu, S. Vempati and S. Ramakrishna, *RSC Adv.*, 2014, **4**, 27979–27987.

23 M. Norek, M. Michalska-Domańska, W. J. Stępniowski, I. Ayala, A. Bombalska and B. Budner, *Appl. Surf. Sci.*, 2013, **287**, 143–149.
24 B. Liu, C. W. Cheng, R. Chen, Z. X. Shen, H. J. Fan and H. D. Sun, *J. Phys. Chem. C*, 2010, **114**, 3407–3410.
25 J. Q. Hu, Y. Bando and D. Golberg, *Chem. Phys. Lett.*, 2003, **372**, 758–762.
26 S. Luo, J. Fan, W. Liu, M. Zhang, Z. Song, C. Lin, X. Wu and P. K. Chu, *Nanotechnology*, 2006, **17**, 1695–1699.
27 S.-S. Chang, S. O. Yoon and H. J. Park, *Ceram. Int.*, 2005, **31**, 405–410.
28 F. Gu, S. F. Wang, C. F. Song, M. K. Lu, Y. X. Qi, G. J. Zhou, D. Xu and D. R. Yuan, *Chem. Phys. Lett.*, 2003, **372**, 451–454.
29 F. Gu, S. F. Wang, M. K. Lu, X. F. Cheng, S. W. Liu, G. J. Zhou, D. Xu and D. R. Yuan, *J. Cryst. Growth*, 2004, **262**, 182–185.
30 Y.-C. Her, J.-Y. Wu, Y.-R. Lin and S.-Y. Tsai, *Appl. Phys. Lett.*, 2006, **89**, 043115.
31 A. Kar, S. Kundu and A. Patra, *J. Phys. Chem. C*, 2011, **115**, 118–124.
32 Ç. Kılıç and A. Zunger, *Phys. Rev. Lett.*, 2002, **88**, 095501.
33 V. J. Babu, M. K. Kumar, A. S. Nair, T. L. Kheng, S. I. Allakhverdiev and S. Ramakrishna, *Int. J. Hydrogen Energy*, 2012, **37**, 8897–8904.
34 V. J. Babu, A. S. Nair, P. Zhu and S. Ramakrishna, *Mater. Lett.*, 2011, **65**, 3064–3068.
35 D. Li and Y. Xia, *Adv. Mater.*, 2004, **16**, 1151–1170.
36 S. S. Lee, H. Bai, Z. Liu and D. D. Sun, *Water Res.*, 2013, **47**, 4059–4073.
37 D. Li and Y. Xia, *Nano Lett.*, 2003, **3**, 555–560.
38 M.-J. Paek, H.-W. Ha, T. W. Kim, S.-J. Moon, J.-O. Baeg, J.-H. Choy and S.-J. Hwang, *J. Phys. Chem. C*, 2008, **112**, 15966–15972.
39 S. Zhang, L.-M. Peng, Q. Chen, G. H. Du, G. Dawson and W. Z. Zhou, *Phys. Rev. Lett.*, 2003, **91**, 256103.
40 R. Ma, Y. Bando and T. Sasaki, *J. Phys. Chem. B*, 2004, **108**, 2115–2119.
41 D. V. Bavykin, V. N. Parmon, A. A. Lapkin and F. C. Walsh, *J. Mater. Chem.*, 2004, **14**, 3370–3377.
42 U. Balachandran and N. G. Eror, *J. Solid State Chem.*, 1982, **42**, 276–282.
43 S. Bakardjieva, V. Stengl, L. Szatmary, J. Subrt, J. Lukac, N. Murafa, D. Niznansky, K. Cizek, J. Jirkovsky and N. Petrova, *J. Mater. Chem.*, 2006, **16**, 1709–1716.
44 L. Abello, B. Bochu, A. Gaskov, S. Koudryavtseva, G. Lucazeau and M. Roumyantseva, *J. Solid State Chem.*, 1998, **135**, 78–85.
45 L. C. Nehru, V. Swaminathan and C. Sanjeeviraja, *Am. J. Mater. Sci.*, 2012, **2**, 6–10.
46 K. N. Yu, Y. Xiong, Y. Liu and C. Xiong, *Phys. Rev. B: Condens. Matter Mater. Phys.*, 1997, **55**, 2666–2671.
47 B. D. Cullity, *Elements of X-ray diffraction*, Addison-Wesley publishing company, Inc., 1956, p. 42.
48 B. D. Cullity, *Elements of X-ray diffraction*, Addison-Wesley publishing company, Inc., 1956, p. 262.
49 L. Z. Liu, T. H. Li, X. L. Wu, J. C. Shen and P. K. Chu, *J. Raman Spectrosc.*, 2012, **43**, 1423–1426.
50 A. K. Tripathi, M. K. Singh, M. C. Mathpal, S. K. Mishra and A. Agarwal, *J. Alloys Compd.*, 2013, **549**, 114–120.
51 A. Maurya, P. Chauhan, S. K. Mishra and R. K. Srivastava, *J. Alloys Compd.*, 2011, **509**, 8433–8440.
52 Y. Cao, W. Yang, W. Zhang, G. Liu and P. Yue, *New J. Chem.*, 2004, **28**, 218–222.
53 T. Hirata, K. Ishioka, M. Kitajima and H. Doi, *Phys. Rev. B: Condens. Matter Mater. Phys.*, 1996, **53**, 8442–8448.
54 G. K. Williamson and W. H. Hall, *Acta Metall.*, 1953, **1**, 22–31.
55 R. R. Prabhu and M. A. Khadar, *Bull. Mater. Sci.*, 2008, **31**, 511–515.
56 E. Wang, T. He, L. Zhao, Y. Chen and Y. Cao, *J. Mater. Chem.*, 2011, **21**, 144–150.
57 A. K. Sinha, P. K. Manna, M. Pradhan, C. Mondal, S. M. Yusuf and T. Pal, *RSC Adv.*, 2014, **4**, 208–211.
58 X. Xu, G. Yang, J. Liang, S. Ding, C. Tang, H. Yang, W. Yan, G. Yang and D. Yu, *J. Mater. Chem. A*, 2014, **2**, 116–122.
59 P. Du, L. Song, J. Xiong, N. Li, Z. Xi, L. Wang, D. Jin, S. Guo and Y. Yuan, *Electrochim. Acta*, 2012, **78**, 392–397.
60 J. Zhang, W. Peng, Z. Chen, H. Chen and L. Han, *J. Mater. Chem. A*, 2013, **1**, 8453–8463.
61 S. K. Zheng, T. M. Wang, W. C. Hao and R. Shen, *Vacuum*, 2002, **65**, 155–159.
62 N. Serpone, D. Lawless and R. Khairutdinov, *J. Phys. Chem.*, 1995, **99**, 16646–16654.
63 P. J. Young, C. Sun-Woo, A. Kandasami and K. S. Sub, *J. Nanosci. Nanotechnol.*, 2010, **10**, 3604–3608.
64 H. Tang, H. Berger, P. E. Schmid and F. Lévy, *Solid State Commun.*, 1993, **87**, 847–850.
65 X. Wu, B. Zou, J. Xu, B. Yut, G. Tang, G. Zhangf and W. Chen, *Nanostruct. Mater.*, 1997, **8**, 179–189.
66 J. Hu, Y. Bando, Q. Liu and D. Golberg, *Adv. Funct. Mater.*, 2003, **13**, 493–496.
67 T. W. Kim, D. U. Lee and Y. S. Yoon, *J. Appl. Phys.*, 2000, **88**, 3759.
68 X. T. Zhou, F. Heigl, M. W. Murphy, T. K. Sham, T. Regier, I. Coulthard and R. I. R. Blyth, *Appl. Phys. Lett.*, 2006, **89**, 213109.
69 M. H. Harunsani, F. E. Oropeza, R. G. Palgrave and R. G. Egdell, *Chem. Mater.*, 2010, **22**, 1551–1558.
70 T. Gao and T. Wang, *Mater. Res. Bull.*, 2008, **43**, 836–842.
71 J. H. He, T. H. Wu, C. L. Hsin, K. M. Li, L. J. Chen, Y. L. Chueh, L. J. Chou and Z. L. Wang, *Small*, 2006, **2**, 116–120.
72 X. Xiang, X. T. Zu, S. Zhu, L. M. Wang, V. Shutthanandan, P. Nachimuthu and Y. Zhang, *J. Phys. D: Appl. Phys.*, 2008, **41**, 225102.
73 H. Shi, M. Zhou, D. Song, X. Pan, J. Fu, J. Zhou, S. Ma and T. Wang, *Ceram. Int.*, 2014, **40**, 10383–10393.